



1 **A fifteen year record of CO emissions constrained by MOPITT CO
2 observations**

3

4 Zhe Jiang^{1,2}, John R. Worden¹, Helen Worden², Merritt Deeter², Dylan B. A. Jones³, Avelino F.
5 Arellano⁴, Daven K. Henze⁵

6

7

8 ¹Jet Propulsion Laboratory, California Institute of Technology, Pasadena, CA, USA

9 ²National Center for Atmospheric Research, Boulder, CO, USA

10 ³Department of Physics, University of Toronto, Toronto, ON, Canada

11 ⁴Department of Hydrology and Atmospheric Sciences, University of Arizona, Tucson, AZ, USA

12 ⁵Department of Mechanical Engineering, University of Colorado, Boulder, CO, USA

13

14

15

16

17

18

19

20

21

22

23

24

25

26

27

28



29 Abstract

30 Long-term measurements from satellites and surface stations have demonstrated a
31 decreasing trend of tropospheric carbon monoxide (CO) in the Northern Hemisphere over the past
32 decade. Likely explanations for this decrease include changes in anthropogenic, fires, and/or
33 biogenic emissions or changes in the primary chemical sink hydroxyl radical (OH). Using
34 remotely sensed CO measurements from the Measurement of Pollution in the Troposphere
35 (MOPITT) satellite instrument, in-situ methyl chloroform (MCF) measurements from World Data
36 Centre for Greenhouse Gases (WDCGG), and the adjoint of the GEOS-Chem model, we estimate
37 the change in global CO emissions from 2001-2015. We show that the loss rate of MCF varies by
38 0.2% in the past 15 years, indicating that changes in global OH distributions do not explain the
39 recent decrease in CO. Our two-step inversion approach for estimating CO emissions is intended
40 to mitigate the effect of bias errors in the MOPITT data as well as model errors in transport and
41 chemistry, which are the primary uncertainties when quantifying CO emissions using these
42 remotely sensed data. Our results confirm that the decreasing trend of tropospheric CO in the
43 Northern Hemisphere is due to decreasing CO emissions from anthropogenic and biomass burning
44 sources. In particular, we find decreasing CO emissions from the United States and China in the
45 past 15 years, unchanged anthropogenic CO emissions from Europe since 2008, and likely a
46 positive trend from India and southeast Asia, in contrast to recently reported results. We find
47 decreasing trends of biomass burning CO emissions from boreal North America, boreal Asia and
48 South America, but little change over Africa. The inconsistency between our analysis with recent
49 study suggests more efforts are needed for robust conclusion about the variation of anthropogenic
50 CO emissions for India and Southeast Asia.



52 **1. Introduction**

53 Tropospheric CO is a product of incomplete combustion and a byproduct of the oxidation
54 of hydrocarbons. It plays a key role in atmospheric chemistry because it is the main sink for OH,
55 and an important precursor for tropospheric ozone (O_3). Recent studies demonstrated significant
56 change in tropospheric CO abundance in the past decade. Using Atmospheric Infrared Sounder
57 (AIRS) CO measurements, Warner et al. (2013) indicated that Northern Hemispheric CO mixing
58 ratio decreased by 1.28 ppb/year in the period of 2003-2012. Worden et al. (2013) demonstrated
59 Northern Hemispheric CO column measurements from MOPITT show a decrease of ~0.92%/year
60 in the period of 2000-2011. Using observations from Mt. Bachelor Observatory, Gratz et al. (2015)
61 also show a negative trend of CO concentration by 1.9%/year in the period of 2004-2013.
62 However, the reason for the large variation of tropospheric CO abundance is still unclear; for
63 example, Strode et al. (2016) found decreases in modeled CO abundance over North America and
64 Europe, but increases over China, based on bottom-up emissions.

65 The budget of tropospheric CO is determined by its sources and sinks. There is currently
66 much effort focused on accurately quantifying emissions of CO. For fossil fuels and biofuels,
67 energy consumption statistics and emission factors are usually used to construct the emission
68 inventories (e.g. Streets et al. 2006; Ohara et al. 2007; Zhang et al. 2009; Zhao et al. 2012).
69 Biomass burning emissions are commonly calculated as the product of burned area, fuel loads,
70 combustion completeness and emission factors (e.g. van der Werf et al. 2006, 2010; van Leeuwen
71 and van der Werf 2011). Because of the large uncertainties in the emission inventories, space-
72 based remotely sensed measurements and surface/aircraft in-situ observations have been
73 assimilated to provide “top-down” constraints on CO emissions (e.g., Arellano et al., 2006;
74 Chevallier et al. 2009; Jones et al., 2009; Kopacz et al., 2010; Jiang et al., 2011; Fortems-Cheiney



75 et al. 2011; Hooghiemstra et al. 2012; Miyazaki et al. 2015). In a recent study, Yin et al. (2015)
76 constrained global CO emissions for the period 2002-2011 to investigate the possible reasons for
77 the decreasing CO abundance in the Northern Hemisphere. Using MOPITT column data (version
78 6J) over the whole globe, Yin et al. (2015) indicate that the negative trend in the Northern
79 Hemisphere is driven by decreasing anthropogenic emissions from North America, Europe and
80 China, similar to our result.

81 The major sink of tropospheric CO is OH. Because of its high variability and short lifetime
82 (about one second), it is difficult to assess the spatial and temporal variation of global OH through
83 direct measurements (Spivakovsky et al. 2000; Lelieveld et al. 2004). Alternatively, Montzka et
84 al. (2011) demonstrated small interannual variability of global OH for the period 1997-2007 by
85 using the loss rate of MCF as a proxy. The measurements of MCF are assimilated in recent CO
86 inversion studies to provide updated OH (e.g. Fortems-Cheiney et al. 2011, 2012; Yin et al. 2015),
87 but the estimates are adversely affected by the sparse distribution of measurements.

88 The objective of this work is to investigate the dominant reasons for the decreasing CO
89 trend in the Northern Hemisphere, and to provide updated CO emission estimates for model studies.
90 Our approach for estimating emissions is intended to reduce the effects of model errors of transport
91 and chemistry, as well as bias errors in the data, on our conclusions about CO emissions; these are
92 the primary uncertainties that affect CO emissions estimates. For example, bias errors as a function
93 of latitude in MOPITT data can have a substantial impact on emissions estimates (Deeter et al.,
94 2014). Model errors of transport and chemistry will have variable and substantial effects on CO
95 emissions in different parts of the globe due to seasonal and latitudinal variations in convection,
96 advection, and boundary layer height (Jiang et al., 2013, 2015a, 2015b).

97 In order to suppress the influences from these systematic measurement and model



98 transport systematic biases, we performed a two-step inversion by combining sequential Kalman
99 Filter (Jiang et al. 2013, 2015a, 2015b) with four-dimensional variational (4D-Var) assimilation
100 (Henze et al. 2007) in this work, using the GEOS-Chem model. Instead of optimizing the CO
101 concentrations and emissions simultaneously (e.g. Fortems-Cheiney et al. 2011, 2012; Yin et al.
102 2015), our first step, the sequential Kalman Filter, modifies the atmospheric CO concentration
103 directly to provide low bias initial (monthly) and boundary (hourly) conditions, whereas the second
104 step (4D-Var) constrains CO emissions assuming perfect initial and boundary conditions. We also
105 apply bias corrections to MOPITT and compare the surface CO concentrations obtained by
106 constraining the model with either MOPITT profile, total column, or lower troposphere data to test
107 which data type provides the most accurate comparison with independent surface in-situ
108 measurements.

109 This paper is organized as follows: in Section 2 we describe the MOPITT instruments and
110 the GEOS-Chem model used in this work. In Section 3 we outline the inverse method. We then
111 investigate the long-term variations of global tropospheric OH and CO emissions in Section 4, and
112 we discuss the changes in tropospheric CO, and the contributions from emissions and
113 meteorological conditions. Our conclusions follow in Section 5.

114 2. Observations and Model

115 2.1. MOPITT

116 The MOPITT instrument was launched on December 18, 1999 on the NASA/Terra
117 spacecraft. The satellite is in a sun-synchronous polar orbit of 705 km and crosses the equator at
118 10:30 local time. The instrument makes measurements in a 612 km cross-track scan with a
119 footprint of 22 km \times 22 km, and provides global coverage every three days. The MOPITT data
120 used here were obtained from the joint (J) retrieval (V6J) of CO from TIR (4.7 μ m) and NIR (2.3 μ m)



121 radiances using an optimal estimation approach (Worden et al., 2010; Deeter et al., 2011). The
122 retrieved volume mixing ratios (VMR) are reported as layer averages of 10 pressure levels (surface,
123 900, 800, 700, 600, 500, 400, 300, 200 and 100 hPa). The relationship between the retrieved CO
124 profile and the true atmospheric state can be described as:

125
$$\hat{z} = z_a + A(z - z_a) + G\varepsilon \quad (1)$$

126 where z_a is the MOPITT a priori CO profile, z is the true atmospheric state, $G\varepsilon$ describes the
127 retrieval error, and $A = \partial\hat{z}/\partial z$ is the MOPITT averaging kernel matrix, which gives the sensitivity
128 of the retrieval to the actual CO in the atmosphere. The MOPITT V6 data have been evaluated by
129 Deeter et al. (2014) using aircraft measurements from HIAPER Pole-to-Pole Observations (HIPPO)
130 and the National Oceanic and Atmospheric Administration (NOAA). For the TIR/NIR multi-
131 spectral retrievals, they found negative bias drift (-1.27%/year) at lower troposphere (800 hPa),
132 and positive bias drift (1.64%/year) at upper troposphere (200 hPa). The bias drift in the total
133 column is negligible (0.003%/year).

134 Figure 1 shows the comparison between MOPITT CO retrievals and HIPPO aircraft
135 measurements. The aircraft measurements are smoothed with MOPITT averaging kernels. The
136 comparison demonstrates a negative bias of MOPITT CO retrievals in the tropics and a positive
137 bias at the middle latitudes in the lower troposphere. Opposite bias is observed in the upper
138 troposphere. Similar latitude dependent biases in remote sensing retrievals have been revealed for
139 methane (CH_4) observations from Scanning Imaging Absorption Spectrometer for Atmospheric
140 Chartography (SCIAMACHY, Bergamaschi et al. 2007, 2009; Meirink et al. 2008), Greenhouse
141 Gases Observing Satellite (GOSAT, Turner et al. 2015), and CO observation from MOPITT
142 (version 4, Hooghiemstra et al. 2012). Similar to previous studies, we reduce the adverse effect of
143 the latitude dependent bias by applying latitude dependent correction factors to MOPITT CO



144 retrievals, based on the black solid line in Figure 1, which represents a 4-order polynomial curve
145 fitting (in a least-squares sense) for all data points.

146 **2.2. GEOS-Chem**

147 The GEOS-Chem global chemical transport model (CTM) [www.geos-chem.org] is driven
148 by assimilated meteorological fields from the NASA Goddard Earth Observing System (GEOS-5)
149 at the Global Modeling and data Assimilation Office. For the simulations in this work, various
150 versions of GEOS meteorological fields are used, including GEOS-4 (2000-2003), GEOS-5 (2004-
151 2012) and GEOS-FP (2013-2015). We use version v35j of the GEOS-Chem adjoint, which is based
152 on v8-02-01 of the forward GEOS-Chem model, with relevant updates through v9-02-01. Our
153 analysis is conducted at a horizontal resolution of $4^\circ \times 5^\circ$ with 47 vertical levels and employs the
154 CO-only simulation in GEOS-Chem, which uses archived monthly OH fields from the full
155 chemistry simulation. The OH fields used in this work are from GEOS-Chem version v5-07-08,
156 with a global annual mean OH concentration of 0.99×10^6 molec/cm³ (Evans et al. 2005). The
157 potential long-term variation of global tropospheric OH is evaluated in section 4.

158 The global anthropogenic emission inventory is from EDGAR 3.2FT2000 (Olivier et al.,
159 2001), but are replaced by the following regional emission inventories: the US Environmental
160 Protection Agency National Emission Inventory (NEI) for 2008 in North America, the Criteria Air
161 Contaminants (CAC) inventory for Canada, the Big Bend Regional Aerosol and Visibility
162 Observational (BRAVO) Study Emissions Inventory for Mexico (Kuhns et al. 2003), the
163 Cooperative Program for Monitoring and Evaluation of the Long-range Transmission of Air
164 Pollutants in Europe (EMEP) inventory for Europe in 2000 (Vestreng et al. 2002) and the INTEX-
165 B Asia emissions inventory for 2006 (Zhang et al. 2009). Biomass burning emissions are based on
166 the Global Fire Emission Database (GFED3, van der Werf et al. 2010). The a priori biomass



167 burning emissions in Sep-Nov 2006 were applied to Sep-Nov 2015 over Indonesia. Additional CO
168 sources come from oxidation of methane and biogenic volatile organic compounds (VOCs) as
169 described in previous studies (Kopacz et al. 2010; Jiang et al. 2013). The biogenic emissions are
170 simulated using the Model of Emissions of Gases and Aerosols from Nature, version 2.0
171 (MEGANv2.0, Guenther et al. 2006). The distribution of the annual mean CO emissions for 2001-
172 2015 is shown in Figure 2. The annual global sources are 892 Tg CO from fossil fuel, biofuel and
173 biomass burning, 623 Tg CO from the oxidation of biogenic VOCs, and 876 Tg CO from the
174 oxidation of CH₄.

175 **3. Inversion Approach**

176 We use the 4D-var data assimilation system in GEOS-Chem (Henze et al. 2007) to
177 constrain the CO sources. In this approach, we minimize the cost function defined as:

$$178 J(x) = \sum_{i=1}^N (F_i(x) - z_i)^T S_{\Sigma}^{-1} (F_i(x) - z_i) + (x - x_a)^T S_a^{-1} (x - x_a)$$

179 where x is the state vector of CO emissions, N is the number of MOPITT observations that are
180 distributed in time over the assimilation period, z_i is a given MOPITT measurement, and $F(x)$ is
181 the forward model. The error estimates are assumed to be Gaussian, and are given by S_{Σ} , the
182 observational error covariance matrix, and S_a , the a priori error covariance matrix, respectively.
183 The Gaussian assumption excludes important systematic errors, such as biases in OH distribution,
184 long-range transport and satellite retrievals in the cost function. Due to lack of meaningful
185 information about the systematic errors, we assume a uniform observation error of 20% without
186 spatial correlation. The combustion CO sources (fossil fuel, biofuel and biomass burning) and the
187 oxidation source from biogenic VOCs are combined together, assuming a 50% uniform a priori
188 error. We optimize the source of CO from the oxidation of CH₄ separately as an aggregated global



189 source, assuming an a priori uncertainty of 25%.

190 Because the 4D-var optimization scheme does not store the full Hessian matrix, we do not
191 construct the a posteriori error covariance matrix, which is the inverse of the Hessian. As opposed
192 to earlier studies using surface measurements, the high spatial density of measurements from
193 satellite instruments can effectively suppress the contribution from random errors in the cost
194 function, leaving systematic errors as the critical factor in the uncertainty. As shown by Heald et
195 al. (2004), different assumptions about the inversion configuration can produce differences in the
196 source estimates that are significantly larger than the a posteriori errors.

197 Removing the bias in initial conditions is essential for inverse analysis, and can be
198 performed with various data assimilation techniques. Model simulations driven by optimized
199 emissions can provide good initial conditions (e.g. Gonzi et al. 2011; Bruhwiler et al. 2014; Deng
200 et al. 2014; Houweling et al. 2014). Alternatively, tracer concentrations can be modified directly
201 to avoid the effect from long-range transport error (e.g. Kopacz et al. 2009; Jiang et al. 2013,
202 2015a). There are also efforts to optimize emissions and concentrations simultaneously (e.g.
203 Fortems-Cheiney et al. 2011, 2012; Bergamaschi et al. 2013; Yin et al. 2015), however, the
204 contributions from emissions and concentrations to model bias may be hard to be distinguished.
205 Figure 3 shows the methodology of our assimilation system. Following our previous studies (Jiang
206 et al. 2013, 2015a, 2015b), we produce initial conditions at the beginning of each monthly
207 assimilation window by assimilating MOPITT data using a sequential Kalman filter. For the results
208 presented here, the Kalman filter assimilation was carried out from March 1, 2000 to December
209 31, 2015.

210 Systematic errors have critical influences on inverse analysis. Jiang et al. (2013) found that
211 the modeled CO concentration from a 10-day forecast simulation have large discrepancy with



212 assimilated CO fields, because of bias in model convective transport. Jiang et al. (2015a)
213 demonstrated that free tropospheric CO is more susceptible to the influences of OH bias than lower
214 tropospheric CO due to the process of long-range transport. On the other hand, Jiang et al. (2015b)
215 indicated that regional inversions have more advantages than global inversions because the
216 boundary conditions can be better controlled. They demonstrated that the systematic bias
217 associated with North American CO emissions due to OH distribution can be reduced by up to 50%
218 with optimized boundary conditions. Similar optimization on the boundary condition can also be
219 employed in global model, for example, Pifster et al. (2005) constrained biomass burning CO
220 emissions from boreal North America with optimized CO fields outside the impacted region.

221 In order to reduce the effects of systematic errors, we designed a two-step inversion to
222 enhance the contributions from local emissions to the discrepancy between model and data, while
223 keeping the influence from long-range transport as low as possible due to sources of uncertainties
224 (e.g. emission uncertainty in the upstream continent, uncertainties in the chemical sink and
225 convective transport in the transport pathway), that are difficult to quantify. As shown in Figure 3,
226 we define the ocean scene (red grids) as boundary conditions. In the first step of our inverse
227 analysis, sequential Kalman filter assimilation, we directly modify CO concentrations without any
228 change to emissions in order to provide an optimized CO fields as consistent as possible with
229 MOPITT. In the second step, the optimized CO fields are used to rewrite CO concentrations over
230 the ocean every hour, while 4D-var inversion is employed to constrain CO emissions, without any
231 change on CO distribution over ocean. Only MOPITT data over land (white grids) were
232 assimilated to constrain CO emissions in the second step. With the fixed/optimized boundary
233 conditions, the global inversion system has been converted to a combination of several regional
234 inversions. Consequently, the emission and transport errors from one continent (e.g. North



235 America) will not affect the emission estimation of another continent (e.g. Europe).

236 **4. Results and Discussion**

237 **4.1. Long-term variation of global tropospheric OH**

238 The distribution of tropospheric OH has significant influence on the inverse analysis of CO
239 emissions (Jiang et al. 2011). Various approaches have been employed to improve the OH
240 distribution in previous studies. Jiang et al. (2013) assimilated MOPITT CO retrievals in full
241 chemistry model simulation to provide updated OH fields. Miyazaki et al. (2015) demonstrated
242 that assimilation of Tropospheric Emission Spectrometer (TES) O₃, Ozone Monitoring Instrument
243 (OMI) NO₂, and MOPITT CO can provide a better description of tropospheric OH. There are also
244 recent efforts that have assimilated surface in-situ MCF measurements (Fortems-Cheiney et al.
245 2011, 2012; Yin et al. 2015). However, because of the uncertainties in model chemistry schemes,
246 potential bias drifts in satellite remotely sensed observation, and sparse distribution of surface in-
247 situ measurements, OH abundances provided by these approaches may not be ideal for the
248 estimation of long-term CO variation.

249 Emissions of MCF are regulated by the Montreal Protocol agreement. The loss rate of MCF
250 has become a good tool to evaluate the variation of tropospheric OH (e.g. Bousquet et al. 2005;
251 Prinn et al. 2005; Montzka et al. 2011). Using the same approach as Montzka et al. (2011), we
252 assess the variation of tropospheric OH in the period of 2001-2015. Figure 4a shows the locations
253 of WDCGG sites with MCF measurements, and Figure 4b shows the global mean MCF
254 concentration in the past 15 years. Similar as Montzka et al. (2011), our result shows a exponential
255 decrease of MCF concentration. The loss rate of MCF, derived from 12-month apart of monthly
256 means [e.g., $\ln(MCF_{Jan2007}/MCF_{Jan2006})$] varies by 0.2% in the past 15 years (Figure 4c). The
257 interannual variation is more likely due to the sparsity and discontinuity of measurements.



258 The small variation of loss rate of MCF demonstrates that the long-term variation of global
259 mean OH distributions is negligible in the past 15 years. Consequently, the decreasing trend of
260 tropospheric CO in North Hemisphere is driven by decreasing CO sources, rather than sinks. For
261 this reason, the default monthly OH fields of GEOS-Chem model (Evans et al. 2005), without
262 interannual variability, are used in this work to constrain the long-term variation of CO emissions.
263 Because the abundances of tropospheric OH have large regional discrepancies (e.g. Jiang et al.
264 2015a), it is possible that the actual OH is more variable at regions lacking MCF measurements
265 (e.g. India and southeast Asia). Futhermore, the magnitude and seasonality of the default monthly
266 OH fields could also have uncertainty. Consequently, the magnitude of CO emissions in our
267 analysis may still be affected by biases in OH, although the two-step assimilation system is
268 designed to suppress their influence.

269 **4.2. Long-term variation of global CO emissions**

270 In this work, we performed monthly inversions for the period of 2001-2015, using
271 MOPITT column, profile and lower tropospheric profile (lowest three retrieval levels) data to
272 investigate the influences associated with vertical sensitivity of satellite instrument and model
273 transport error. Figure 5 shows the CO emission trends for 2001-2015 constrained by these
274 different datasets. For anthropogenic sources, all three analysis show significant emission
275 reduction from North America, Europe and China. The emission estimates constrained with
276 MOPITT column and profile data demonstrate increasing CO emissions from India and Southeast
277 Asia. Conversely, the emission estimate constrained with MOPITT lower tropospheric profile data
278 shows a decreasing trend in this region, and this decreasing trend is also obtained by Yin et al.
279 (2015). As shown in Jiang et al., (2013), errors in model convection in this region have a large
280 effect on CO emissions estimates, and information about the vertical profile of CO has a stronger



281 influence on the results.

282 For biomass burning sources, we found a negative trend over boreal North America, boreal
283 Asia and South America, and a positive trend over Indonesia that is primarily due to the strong
284 impacts of El Nino in 2006 and 2015 on biomass burning in this region (e.g. Field et al., 2016).
285 Our results for biogenic VOCs are inconclusive; the emission estimates constrained with MOPITT
286 column and profile data show moderate positive trends in the tropics, and slight negative trends in
287 mid-latitude regions, whereas the emission estimate constrained with MOPITT lower tropospheric
288 profile data shows a negative trend globally.

289 Figure 6a shows the regional variation of anthropogenic emissions from the United States
290 (US). The emission estimates constrained with MOPITT column and profile data match very well
291 with the a priori emissions, whereas the emission estimate constrained with MOPITT lower
292 tropospheric profile data is much higher. All three analyses demonstrate a significant emission
293 reduction over our study period. As shown in Table 1, the total anthropogenic CO emission
294 (constrained with MOPITT profile data) from US is 56.8 Tg in 2015, which is 35% lower than that
295 in 2001 (87.7 Tg). Figure 7a shows the monthly mean CO concentrations from WDCGG stations
296 in US, which demonstrates a similar decreasing trend as our analysis. The decreasing trend is
297 consistent with the US Environmental Protection Agency (EPA) Emissions Trends Data
298 (<https://www.epa.gov/air-emissions-inventories/air-pollutant-emissions-trends-data>), and other
299 observation records for western US (Gratz et al. 2015), southeast US (Hidy et al. 2014) and North
300 Atlantic (Kumar et al. 2013).

301 Figure 6b shows the regional variation of anthropogenic emissions from Europe. All three
302 analyses show an underestimation of a priori emissions, suggesting the CO emissions in the EMEP
303 inventory are too low. Our results show that anthropogenic emissions decrease during the period



304 of 2001-2007, but are almost unchanged in the following years, which is consistent with the
305 observations from WDCGG stations (Figure 7b). Recent studies (Hilboll et al. 2013; Schneider et
306 al. 2015) showed that NO₂ over Europe from SCIAMACHY is decreasing in the period of 2002-
307 2008, and almost unchanged in the period of 2008-2011. Henschel et al. (2015) indicated that the
308 unchanged NO₂ over Europe could be caused by European emissions that are failing to achieve
309 the expected reduction standards. Because anthropogenic CO and NO₂ share some of the same
310 combustion sources, it is possible that the unchanged CO emission in our analysis is also due to a
311 failure of emission controls.

312 Figure 6c shows the regional variation of anthropogenic emissions from east China. We
313 found Chinese anthropogenic emissions are increasing in the period of 2001-2004. Accompanied
314 with the global economy recession, the total anthropogenic CO emission (constrained with
315 MOPITT profile data) from east China decreases to 175.4 Tg in 2008, which is 15% lower than
316 that in 2004 (205.6 Tg). Our analysis shows a temporary increase of Chinese emissions in 2009
317 (185.9 Tg), followed by continuous decrease. The total Chinese anthropogenic CO emission is
318 159.0 Tg in 2015, which is 7% lower than that in 2001 (170.4 Tg). Using surface in-situ
319 measurements at Hateruma Island, Tohjima et al. (2014) constrained CO emissions from China
320 for the period 1999-2010. They found Chinese CO emission increases from 1999-2004, and
321 decreases since 2005. Using a “bottom-up” approach, recent studies (Zhao et al. 2012; Xia et al.
322 2016) indicated that the growth trend of Chinese CO emissions has been changed since 2005
323 because of improvements in energy efficiency and emission control regulations (e.g. Liu et al.
324 2015). Figure 7c shows the observation records from 2 stations in the East China outflow region,
325 which demonstrate similar variations.

326 Figures 6d-6e show the regional variation of anthropogenic emissions from India and



327 Southeast Asia. The emission estimates constrained with MOPITT column and profile data
328 demonstrate significant positive trend in our study period, whereas the emission estimate
329 constrained with MOPITT lower tropospheric profile data shows a decreasing trend. Schneider et
330 al. (2015) showed that NO₂ over south Asia from SCIAMACHY is increasing in the period of
331 2003-2011. Using OMI NO₂ measurements, recent studies (e.g., Duncan et al. 2016) demonstrated
332 that NO₂ over India has a positive trend during 2005-2015. Observations from Cape Rama (CRI)
333 station (Figure 7d) demonstrate that CO concentration in 2010-2013 is significantly higher than
334 that in 2001-2002. For these reasons, we have more confidence in our results that indicate
335 increasing anthropogenic CO emissions from India and Southeast Asia in the past 15 years. The
336 trend based on the MOPITT lower-tropospheric data is incorrect because of model error in
337 convection and boundary layer height in this dynamically varying region, and the negative bias
338 drift in MOPITT lower tropospheric retrievals (Deeter et al., 2014). The total anthropogenic CO
339 emission (constrained with MOPITT profile data) from India and Southeast Asia is 130.4 Tg in
340 2015, which is 34% higher than that in 2001 (97.5 Tg). It should be noted that the inconsistency
341 between our analysis with Yin et al. (2015) suggests more studies are needed for robust conclusion
342 about the variation of anthropogenic CO emissions for this region.

343 Although our inverse analysis (constrained with MOPITT profile data) suggests similar
344 anthropogenic CO emissions from East China in 2008 and 2014, Figure 7c demonstrates that mean
345 CO concentrations over the outflow region of East China are 6 ppb higher in 2014 compared to
346 2008. Our previous study (Jiang et al. 2015c) indicated that anthropogenic emissions from India
347 and southeast Asia have an important influence on pollutant concentrations in the east China
348 outflow region. It is possible that the increase of CO concentration observed by WDCGG stations
349 in this region is caused by the significant increase of anthropogenic CO emission from India and



350 southeast Asia. In the most recent 5 years (2011-2015), our results (constrained with MOPITT
351 profile data) suggested a 20.5 Tg emission reduction from East China, and a 10.1 Tg emission
352 increase from India and Southeast Asia. Assuming a fixed emission growth rate, projected
353 anthropogenic CO emissions from India and Southeast Asia will overtake Chinese emissions in
354 2020, resulting in serious socioeconomic issues on both local and global scales.

355 Figure 8 shows the regional variation of biomass burning emissions. There are significant
356 decreasing trends in three regions (i.e. boreal North America, boreal Asia, and South America).
357 Our results show high biomass burning emissions from boreal North America (mainly Alaska and
358 western Canada) in 2004 (Figure 8a), which have been reported by previous studies (e.g. Pfister et
359 al. 2005; Turquety et al. 2007), and also from boreal Asia during 2001-2003 (Figure 8b) due to
360 significant fire activity in Siberia (e.g., Yurganov et al., 2005, Stroppiana et al., 2010). For South
361 America (Figure 8c), we found higher biomass burning emissions in the periods of 2004-2007 and
362 2010, consistent with fire activity reported in previous studies (e.g. Hooghiemstra et al. 2012;
363 Bloom et al. 2015).

364 Figure 8d shows the regional variation of biomass burning emissions from Africa. The fire
365 activities in Africa demonstrates obvious seasonality: peak in boreal winter for Northern
366 Hemispheric Africa, and in austral winter for Southern Hemispheric Africa. Similar to previous
367 studies (e.g. Chevallier et al. 2009; Tosca et al. 2015), there is no obvious emission trend in Africa
368 in the past 15 years. This is also consistent with the burned area trends described by Andela et al.
369 (2014) which show opposite directions for Northern Africa (decreasing) versus Southern Africa
370 (increasing) and would have cancelling effects in the trend for the continent as a whole.

371 Our results exhibit two strong biomass burning events in Indonesia, 2006 and 2015,
372 individually (Figure 8e). Previous studies (e.g. Logan et al. 2008; Zhang et al. 2011; Worden et al.



373 2013b, 2013c, Field et al., 2016) demonstrate the direct relationship between strong Indonesian
374 fires and El Niño. More recent studies (Huang et al. 2014; Inness et al. 2015) confirm low biomass
375 burning activities in Indonesia in the period of 2007-2012. CO emissions from the Indonesian fires
376 associated with the 2015 El Niño were 92 Tg, (for October, 2015, as constrained with MOPITT
377 profile data), and were about three times higher than the October 2006 El Niño driven fire
378 emissions (32 Tg). Not including the 2015 El Niño driven fires, our analysis indicates a negative
379 trend of global biomass burning emissions in the past 15 years, as shown in Figure 11f.

380 **4.3. Changes in tropospheric CO during 2001-2015**

381 In this section, we evaluate our inversion results using independent long-term surface in-
382 situ measurements from WDCGG stations. Figure 9a shows the annual trend of surface CO
383 concentration for 2001 – 2015 from WDCGG sites, and from model simulations driven with a
384 priori emissions. Most WDCGG sites exhibit negative trends in the past 15 years, confirming the
385 decreasing trend of global tropospheric CO, which is consistent with satellite observations (e.g.
386 Warner et al. 2013; Worden et al. 2013). There are also stations with positive trends, for example,
387 Tae-ahn Peninsula (TAP, Korea), Ascension Island (ASC, equatorial Atlantic Ocean), Cape Rama
388 (CRI, India), Bukit Koto Tabang (BKT, Indonesia) and Cape Grim (CGO, Australia). Globally,
389 the a priori model simulation is in reasonable agreement with WDCGG measurements: both show
390 negative trends in middle/high latitude, and positive trends in some tropical regions. However,
391 there are noticeable discrepancies, for example, the surface observation from Yonagunijima (YON,
392 east China sea) shows a negative trend in our study period, suggesting decreasing trend from
393 Chinese CO emission, whereas the a priori simulation demonstrates significant positive trend.

394 Figure 9b-9d show the model simulations driven with a posteriori emissions. The a
395 posteriori emissions constrained with MOPITT lower tropospheric profile data (Figure 9d) results



396 in unrealistic large CO reduction, which could be caused by the negative bias drift of MOPITT
397 retrievals at lower troposphere (Deeter et al. 2014) and the influence from possible variability in
398 model convective transport. The a posteriori emissions constrained with MOPITT column and
399 profile data have similar comparisons. For example, both of them suggest a negative trend over
400 east China, consistent with observations from YON, and positive trend over northeast Asia,
401 consistent with observations from TAP.

402 In order to better compare the discrepancy between model simulation and surface
403 observations, Figure 9e-9g show the improvement due to a posteriori emissions, derived by
404 $\text{abs}(\text{Trend}_{\text{a posteriori}} - \text{Trend}_{\text{WDCGG}}) - \text{abs}(\text{Trend}_{\text{a priori}} - \text{Trend}_{\text{WDCGG}})$. Blue (red) means the a posteriori
405 emissions improves (degrades) the agreement with WDCGG measurements compared to the
406 simulated surface CO using a priori emissions, while white indicates no change from the prior. As
407 shown in Figure 9f, the CO emissions constrained with MOPITT profile data improved the model
408 simulation for most WDCGG sites in the Northern Hemisphere. The a posteriori emissions
409 constrained with MOPITT column data are somewhat worse, particularly over Europe, while CO
410 emissions constrained with MOPITT profile data over Europe give improved comparisons to
411 WDCGG surface CO measurements. Worden et al. (2010) demonstrated that the degrees of
412 freedom for signal (DFS) of MOPITT multi-spectral profile retrievals (TIR+NIR) is about 1.5-2.0
413 over land, which is reduced to about 1 DFS when converted to a total column. This reduction in
414 vertical information in MOPITT column data can affect the the reliability of inverse analysis
415 results (Jiang et al., 2015a). It should be noticed that the vertical correlation in model simulation
416 is not considered in our assimilation, which could be another possible reason for this discrepancy.

417 Figure 10a-10d show the long-term mean value of surface CO concentration for 2001 –
418 2015 from WDCGG sites, and model simulations driven with a priori and a posteriori emissions.



419 All simulations provide similar results for long-term mean value. Figure 10e-10g show the
420 improvement due to a posteriori emissions, derived by $\text{abs}(\text{CO}_{\text{aposteriori}} - \text{CO}_{\text{WDCGG}}) - \text{abs}(\text{CO}_{\text{apriori}}$
421 - $\text{CO}_{\text{WDCGG}})$. Figure 10f demonstrates that CO emissions constrained with MOPITT profile data
422 improved the model simulation in about half of the sites in the Northern Hemisphere, whereas the
423 a posteriori emissions constrained with MOPITT column data are somewhat worse (Figure 10e).
424 Evaluating modeled tracer concentrations using surface in-situ measurements is more challenging
425 than evaluating long-term trends. In a recent study, Schnell et al. (2015) evaluate surface O_3
426 concentrations simulated by multi-models for North America and Europe. They found most
427 models can provide good simulations for the patterns of O_3 but cannot reproduce the magnitude.
428 Important sources of uncertainty include the representation error (e.g. Chang et al. 2015; Kharol
429 et al. 2015) and vertical mixing of boundary layer (e.g. Castellanos et al. 2011; Cuchiara et al.
430 2014).

431 Because our a posteriori simulation, particularly using emissions constrained with
432 MOPITT profile data, results in significant improvement in the long-term trend, and moderate
433 improvement in the mean value, we believe these a posteriori estimates provide a better description
434 for the long-term variation of global CO emissions. A remaining question is to explore how
435 changes in meterological conditions affect the long-term variation. By fixing CO emissions to
436 2001 levels, Figure 11a-11b show the long-term trend of modeled surface and column CO during
437 2001-2015, due only to changes in meterological conditions. At the surface level (Figure 11a), we
438 found changes in meterology result in a moderate positive trend in the Northern Hemisphere,
439 particularly, over northeast Asia, consistent with observation records from the TAP station; and
440 significant positive trend in tropics, consistent with observation record from ASC station. On the
441 other hand, the influence of meterological conditions on column CO (Figure 11b) is much weaker.



442 The discrepancy between surface and column CO suggests the possible contribution from variable
443 convective transport, which could be associated with changes in the frequency of deep convection
444 (Tan et al. 2015) or the change from El Niño to La Niña in our study period (Andela et al. 2014).
445 In order to assess the influence of various versions of the meterological fields (i.e. GEOS-4, GEOS-
446 5 and GEOS-FP) on the trend analysis, we replotted (not shown) Figure 11a-11b for the period
447 2004-2012 with GEOS-5 meterological fields, and obtained similar significant positive trend in
448 tropics, which suggests limited influence from meterological field version differences on the trend
449 analysis.

450 Figure 11c-11h show the variation of global tropospheric CO due to changes in emissions.
451 Yin et al. (2015) indicated that the negative trend of tropospheric CO in the Northern Hemisphere
452 is driven by decreasing anthropogenic emissions from North America, Europe and China. Along
453 with reductions in anthropogenic emissions (Figure 11c, 11d), we found the decrease of biomass
454 burning emissions from boreal North America and boreal Asia (Figure 11e, 11f) to be an important
455 factor for this negative trend. In contrast to the emission reduction from North America, Europe
456 and China, we found increasing anthropogenic emissions from India and southeast Asia, which
457 result in a pronounced positive trend of tropospheric CO, while Yin et al. (2015) obtain a negative
458 trend for this region. This discrepancy requires further study and we will need to test the relative
459 importance of the primary differences in our methods, i.e., models and inversion approaches,
460 climatological OH (this study) vs. assimilated surface measurements of CH₄ and MCF to update
461 OH (Yin et al.) and the use of MOPITT profile vs. column CO retrievals (Yin et al., assimilate
462 only column CO).

463 **5. Summary**

464 The objective of this work is to investigate the dominant reasons for the observed variation



465 of global tropospheric CO over the past 15 years, and to provide updated CO emission estimates
466 for model studies. In particular, we use a combination of MOPITT CO measurements and surface
467 measurements of MCF to evaluate changes in the sources and sinks of atmospheric CO, with the
468 goal of explaining the observed decrease in CO concentrations. Our two-step approach for
469 estimating global CO emissions mitigates the effects of model errors from transport and chemistry,
470 as well as measurement bias error.

471 Using the same approach as Montzka et al. (2011), we assess the variation of tropospheric
472 OH (the primary CO sink) in the period of 2001-2015 using MCF measurements from WDCGG
473 stations. Our result demonstrates negligible variation of global tropospheric OH in the past 15
474 years, and consequently we suggest that the global sink of CO due to chemical loss through OH
475 has not likely changed during this time period. We therefore expect the decreasing trend of
476 tropospheric CO in North hemisphere (e.g. Warner et al. 2013; Worden et al. 2013; Gratz et al.
477 2015) to be driven by decreasing CO sources. Total anthropogenic CO emissions from the US
478 were 56.8 Tg in 2015, which are 35% lower than emissions in 2001 (87.7 Tg). Total anthropogenic
479 CO emissions from East China were 159.0 Tg in 2015, which are 7% lower than 2001 emissions
480 (170.4 Tg) and 23% lower than 2004 emissions (205.6 Tg). This pronounced decrease of emissions
481 from US and China is an indication of progress for fuel efficiency and emission control regulations.
482 Conversely, our results demonstrate that anthropogenic emissions from Europe decreased from
483 2001 to 2007 but are almost unchanged during 2008-2015. We also found a significant increase of
484 anthropogenic emissions for India and Southeast Asia. The total anthropogenic CO emission from
485 India and southeast Asia is 130.4 Tg in 2015, which is 34% higher than that in 2001 (97.5 Tg).
486 Assuming the same emission growth rate as 2011-2015, we expect that anthropogenic CO
487 emissions from India and Southeast Asia will be larger than Chinese emissions by 2020.



488 In a recent study, Yin et al. (2015) indicated that the decreasing tropospheric CO in the
489 Northern Hemisphere is caused by the decrease of anthropogenic emissions from North America,
490 Europe and China. We find that a decrease of biomass burning emissions from boreal North
491 America and boreal Asia is also an important contributor for the negative trend. Globally, our
492 analysis indicates a negative trend of biomass burning emissions in the past 15 years, except in
493 Indonesia due to the strong biomass burning event in 2015 associated with El Niño. Our results
494 demonstrate a significant decrease of biomass burning emissions from South America, which
495 could be associated with the reduction of deforestation in Brazil (Reddington et al. 2015), and the
496 predominant change from El Niño to La Niña in our study period (Andela et al. 2014). For Africa,
497 there is no obvious CO emission trend in the past 15 years, consistent with previous results
498 (Chevallier et al. 2009; Tosca et al. 2015; Andela et al., 2014). Our results are inconclusive in
499 characterizing the CO sources from oxidation of biogenic VOCs. More efforts are needed in the
500 future to better understand the mechanism for tropical CO emissions.

501 Our analysis highlights the importance of space-based instruments for monitoring changes
502 in global pollutant emissions. Our results demonstrate successful emission controls in US and
503 China over the past 15 years, and suggest that emission controls in Europe may need re-evaluation.
504 We also recommend more efforts in the future to better understand the regional and global effects
505 of increasing pollutant emissions from India and Southeast Asia.

506

507 **Acknowledgments.**

508 We thank the World Data Centre for Greenhouse Gases (WDCGG) for providing their CO
509 and MCF data. The National Center for Atmospheric Research (NCAR) is sponsored by the
510 National Science Foundation. The NCAR MOPITT project is supported by the National



511 Aeronautics and Space Administration (NASA) Earth Observing System (EOS) Program. The
512 MOPITT team also acknowledges support from the Canadian Space Agency (CSA), the Natural
513 Sciences and Engineering Research Council (NSERC) and Environment Canada, along with the
514 contributions of COMDEV (the prime contractor) and ABB BOMEM. MOPITT data sets used in
515 this study are publicly available at <http://reverb.echo.nasa.gov> and at
516 <https://eosweb.larc.nasa.gov/datapool>.

517

518 **Data availability**

519 The MOPITT data is available at <ftp://l5eil01.larc.nasa.gov/MOPITT/MOP02J.006>. The MCF and
520 CO measurements from WDCGG is available at <http://ds.data.jma.go.jp/gmd/wdcgg/>.

521

522 **References**

523 Arellano, A., Kasibhatla, P., Giglio, L., Werf, G., Randerson, J. and Collatz, G.: Time-dependent
524 inversion estimates of global biomass-burning CO emissions using Measurement of Pollution in
525 the Troposphere (MOPITT) measurements, J Geophys Res Atmospheres 1984 2012, 111(D9),
526 doi:10.1029/2005JD006613, 2006.

527 Andela, N., and van der Werf, G.: Recent trends in African fires driven by cropland expansion and
528 El Niño to La Niña transition, Nature Climate Change 4, 791–795, doi:10.1038/nclimate2313,
529 2014.

530 Bergamaschi, P., Frankenberg, C., Meirink, J., Krol, M., Dentener, F., Wagner, T., Platt, U.,
531 Kaplan, J., Körner, S., Heimann, M., Dlugokencky, E. and Goede, A.: Satellite chartography of
532 atmospheric methane from SCIAMACHY on board ENVISAT: 2. Evaluation based on inverse
533 model simulations, J Geophys Res Atmospheres 1984 2012, 112(D2),



534 doi:10.1029/2006JD007268, 2007.

535 Bergamaschi, P., Frankenberg, C., Meirink, J., Krol, M., Villani, M., Houweling, S., Dentener, F.,
536 Dlugokencky, E., Miller, J., Gatti, L., Engel, A. and Levin, I.: Inverse modeling of global and
537 regional CH₄ emissions using SCIAMACHY satellite retrievals, *J Geophys Res Atmospheres*
538 1984 2012, 114(D22), doi:10.1029/2009JD012287, 2009.

539 Bergamaschi, P., Houweling, S., Segers, A., Krol, M., Frankenberg, C., Scheepmaker, R.,
540 Dlugokencky, E., Wofsy, S., Kort, E., Sweeney, C., Schuck, T., Brenninkmeijer, C., Chen, H.,
541 Beck, V. and Gerbig, C.: Atmospheric CH₄ in the first decade of the 21st century: Inverse
542 modeling analysis using SCIAMACHY satellite retrievals and NOAA surface measurements, *J*
543 *Geophys Res Atmospheres*, 118(13), 7350–7369, doi:10.1002/jgrd.50480, 2013.

544 Bloom, A., Worden, J., Jiang, Z., Worden, H., Kurosu, T., Frankenberg, C. and Schimel, D.:
545 Remote-sensing constraints on South America fire traits by Bayesian fusion of atmospheric and
546 surface data, *Geophys Res Lett*, 42(4), 1268–1274, doi:10.1002/2014GL062584, 2015.

547 Bousquet, P., Hauglustaine, D. A., Peylin, P., Carouge, C., and Ciais, P.: Two decades of OH
548 variability as inferred by an inversion of atmospheric transport and chemistry of methyl
549 chloroform, *Atmos. Chem. Phys.*, 5, 2635–2656, doi:10.5194/acp-5-2635-2005, 2005.

550 Bruhwiler, L., Dlugokencky, E., Masarie, K., Ishizawa, M., Andrews, A., Miller, J., Sweeney, C.,
551 Tans, P., and Worthy, D.: CarbonTracker-CH₄: an assimilation system for estimating emissions
552 of atmospheric methane, *Atmos. Chem. Phys.*, 14, 8269–8293, doi:10.5194/acp-14-8269-2014,
553 2014.

554 Castellanos, P., Marufu, L., Doddridge, B., Taubman, B., Schwab, J., Hains, J., Ehrman, S. and
555 Dickerson, R.: Ozone, oxides of nitrogen, and carbon monoxide during pollution events over the
556 eastern United States: An evaluation of emissions and vertical mixing, *J Geophys Res*



557 Atmospheres 1984 2012, 116(D16), doi:10.1029/2010JD014540, 2011.

558 Chang, K.-L., Guillas, S., and Fioletov, V. E.: Spatial mapping of ground-based observations of
559 total ozone, Atmos. Meas. Tech., 8, 4487-4505, doi:10.5194/amt-8-4487-2015, 2015.

560 Chevallier, F., Fortems, A., Bousquet, P., Pison, I., Szopa, S., Devaux, M. and Hauglustaine, D.:
561 African CO emissions between years 2000 and 2006 as estimated from MOPITT observations,
562 Biogeosciences, 6(1), 103–111, doi:10.5194/bg-6-103-2009, 2009.

563 Cuchiara, G. C., Li, X., Carvalho, J. and Rappenglück, B.: Intercomparison of planetary boundary
564 layer parameterization and its impacts on surface ozone concentration in the WRF/Chem model
565 for a case study in Houston/Texas, Atmos. Environ., 96, 175–185,
566 doi:10.1016/j.atmosenv.2014.07.013, 2014.

567 Deeter, M., Worden, H., Gille, J., Edwards, D., Mao, D. and Drummond, J.: MOPITT multispectral
568 CO retrievals: Origins and effects of geophysical radiance errors, J Geophys Res Atmospheres
569 1984 2012, 116(D15), doi:10.1029/2011JD015703, 2011.

570 Deeter, M. N., Martínez-Alonso, S., Edwards, D. P., Emmons, L. K., Gille, J. C., Worden, H. M.,
571 Sweeney, C., Pittman, J. V., Daube, B. C., and Wofsy, S. C.: The MOPITT Version 6 product:
572 algorithm enhancements and validation, Atmos. Meas. Tech., 7, 3623-3632, doi:10.5194/amt-7-
573 3623-2014, 2014.

574 Deng, F., Jones, D. B. A., Henze, D. K., Bousserez, N., Bowman, K. W., Fisher, J. B., Nassar, R.,
575 O'Dell, C., Wunch, D., Wennberg, P. O., Kort, E. A., Wofsy, S. C., Blumenstock, T., Deutscher,
576 N. M., Griffith, D. W. T., Hase, F., Heikkinen, P., Sherlock, V., Strong, K., Sussmann, R., and
577 Warneke, T.: Inferring regional sources and sinks of atmospheric CO₂ from GOSAT XCO₂ data,
578 Atmos. Chem. Phys., 14, 3703-3727, doi:10.5194/acp-14-3703-2014, 2014.

579 Duncan, B., Lamsal, L., Thompson, A., Yoshida, Y., Lu, Z., Streets, D., Hurwitz, M. and



580 Pickering, K.: A space-based, high-resolution view of notable changes in urban NO_x pollution
581 around the world (2005–2014), *J Geophys Res Atmospheres*, 121(2), 976–996,
582 doi:10.1002/2015JD024121, 2016.

583 Evans, M. J., and Jacob, D. J.: Impact of new laboratory studies of N₂O₅ hydrolysis on global
584 model budgets of tropospheric nitrogen oxides, ozone, and OH, *Geophys. Res. Lett.*, 32, L09813,
585 doi:10.1029/2005GL022469, 2005.

586 Field, R. et al., 2015 Indonesian fire activity and smoke pollution show persistent non-linear
587 sensitivity to El Niño-induced drought, *PNAS*, 2016, 9204–9209, doi: 10.1073/pnas.1524888113

588 Fortems-Cheiney, A., Chevallier, F., Pison, I., Bousquet, P., Szopa, S., Deeter, M. and Clerbaux,
589 C.: Ten years of CO emissions as seen from Measurements of Pollution in the Troposphere
590 (MOPITT), *J Geophys Res Atmospheres* 1984–2012, 116(D5), doi:10.1029/2010JD014416,
591 2011.

592 Fortems-Cheiney, A., Chevallier, F., Pison, I., Bousquet, P., Saunois, M., Szopa, S., Cressot, C.,
593 Kurosu, T. P., Chance, K., and Fried, A.: The formaldehyde budget as seen by a global-scale
594 multi-constraint and multi-species inversion system, *Atmos. Chem. Phys.*, 12, 6699–6721,
595 doi:10.5194/acp-12-6699-2012, 2012.

596 Gonzi, S., Feng, L. and Palmer, P.: Seasonal cycle of emissions of CO inferred from MOPITT
597 profiles of CO: Sensitivity to pyroconvection and profile retrieval assumptions, *Geophys. Res.*
598 *Lett.*, 38(8), n/a–n/a, doi:10.1029/2011GL046789, 2011.

599 Gratz, L. E., Jaffe, D. A. and Hee, J. R.: Causes of increasing ozone and decreasing carbon
600 monoxide in springtime at the Mt. Bachelor Observatory from 2004 to 2013, *Atmos. Environ.*,
601 109, 323–330, doi:10.1016/j.atmosenv.2014.05.076, 2015.

602 Guenther, A., Karl, T., Harley, P., Wiedinmyer, C., Palmer, P.I., and Geron, C.: Estimates of global



603 terrestrial isoprene emissions using MEGAN (Model of Emissions of Gases and Aerosols from
604 Nature), Atmos. Chem. Phys., 6, 3181-3210, doi:10.5194/acp-6-3181-2006, 2006.

605 Heald, C., Jacob, D., Jones, D., Palmer, P., Logan, J., Streets, D., Sachse, G., Gille, J., Hoffman,
606 R. and Nehrkorn, T.: Comparative inverse analysis of satellite (MOPITT) and aircraft (TRACE-
607 P) observations to estimate Asian sources of carbon monoxide, J Geophys Res Atmospheres 1984
608 2012, 109, D23306, doi:10.1029/2004JD005185, 2004.

609 Henze, D. K., Hakami, A., and Seinfeld, J. H.: Development of the adjoint of GEOS-Chem, Atmos.
610 Chem. Phys., 7, 2413-2433, doi:10.5194/acp-7-2413-2007, 2007.

611 Hilboll, A., Richter, A., and Burrows, J. P.: Long-term changes of tropospheric NO₂ over
612 megacities derived from multiple satellite instruments, Atmos. Chem. Phys., 13, 4145-4169,
613 doi:10.5194/acp-13-4145-2013, 2013.

614 Hidy, G., Blanchard, C., Baumann, K., Edgerton, E., Tanenbaum, S., Shaw, S., Knipping, E.,
615 Tombach, I., Jansen, J. and Walters, J.: Chemical climatology of the southeastern United States,
616 1999–2013, Atmos Chem Phys, 14(21), 11893–11914, doi:10.5194/acp-14-11893-2014, 2014.

617 Hooghiemstra, P., Krol, M., Leeuwen, T., Werf, G., Novelli, P., Deeter, M., Aben, I. and
618 Röckmann, T.: Interannual variability of carbon monoxide emission estimates over South
619 America from 2006 to 2010, J Geophys Res Atmospheres 1984 2012, 117(D15), n/a–n/a,
620 doi:10.1029/2012JD017758, 2012.

621 Houweling, S., Krol, M., Bergamaschi, P., Frankenberg, C., Dlugokencky, E. J., Morino, I.,
622 Notholt, J., Sherlock, V., Wunch, D., Beck, V., Gerbig, C., Chen, H., Kort, E. A., Röckmann,
623 T., and Aben, I.: A multi-year methane inversion using SCIAMACHY, accounting for
624 systematic errors using TCCON measurements, Atmos. Chem. Phys., 14, 3991-4012,
625 doi:10.5194/acp-14-3991-2014, 2014.



626 Jiang, Z., Jones, D., Kopacz, M., Liu, J., Henze, D. and Heald, C.: Quantifying the impact of model
627 errors on top-down estimates of carbon monoxide emissions using satellite observations, J
628 Geophys Res Atmospheres 1984 2012, 116(D15), doi:10.1029/2010JD015282, 2011.

629 Jiang, Z., Jones, D., Worden, H., Deeter, M., Henze, D., Worden, J., Bowman, K., Brenninkmeijer,
630 C. and Schuck, T.: Impact of model errors in convective transport on CO source estimates
631 inferred from MOPITT CO retrievals, J Geophys Res Atmospheres, 118(4), 2073–2083,
632 doi:10.1002/jgrd.50216, 2013.

633 Jiang, Z., Jones, D., Worden, H. and Henze, D.: Sensitivity of top-down CO source estimates to
634 the modeled vertical structure in atmospheric CO, Atmos Chem Phys, 15(3), 1521–1537,
635 doi:10.5194/acp-15-1521-2015, 2015a.

636 Jiang, Z., Jones, D., Worden, J., Worden, H., Henze, D. and Wang, Y.: Regional data assimilation
637 of multi-spectral MOPITT observations of CO over North America, Atmos Chem Phys, 15(12),
638 6801–6814, doi:10.5194/acp-15-6801-2015, 2015b.

639 Jiang, Z., Worden, J. R., Jones, D. B. A., Lin, J.-T., Verstraeten, W. W., and Henze, D. K.:
640 Constraints on Asian ozone using Aura TES, OMI and Terra MOPITT, Atmos. Chem. Phys., 15,
641 99–112, doi:10.5194/acp-15-99-2015, 2015c.

642 Jones, D., Bowman, K., Logan, J., Heald, C., Liu, J., Luo, M., Worden, J. and Drummond, J.: The
643 zonal structure of tropical O₃ and CO as observed by the Tropospheric Emission Spectrometer
644 in November 2004 – Part 1: Inverse modeling of CO emissions, Atmos Chem Phys, 9(11), 3547–
645 3562, doi:10.5194/acp-9-3547-2009, 2009.

646 Henschel, S., Tertre, A., Atkinson, R., Querol, X., Pandolfi, M., Zeka, A., Haluza, D., Analitis, A.,
647 Katsouyanni, K., Bouland, C., Pascal, M., Medina, S. and Goodman, P.: Trends of nitrogen
648 oxides in ambient air in nine European cities between 1999 and 2010, Atmos Environ, 117, 234–



649 241, doi:10.1016/j.atmosenv.2015.07.013, 2015.

650 Huang, L., Fu, R., and Jiang, J. H.: Impacts of fire emissions and transport pathways on the
651 interannual variation of CO in the tropical upper troposphere, *Atmos. Chem. Phys.*, 14, 4087-
652 4099, doi:10.5194/acp-14-4087-2014, 2014.

653 Inness, A., Benedetti, A., Flemming, J., Huijnen, V., Kaiser, J. W., Parrington, M., and Remy, S.:
654 The ENSO signal in atmospheric composition fields: emission-driven versus dynamically
655 induced changes, *Atmos. Chem. Phys.*, 15, 9083-9097, doi:10.5194/acp-15-9083-2015, 2015.

656 Kopacz, M., Jacob, D., Henze, D., Heald, C., Streets, D. and Zhang, Q.: Comparison of adjoint
657 and analytical Bayesian inversion methods for constraining Asian sources of carbon monoxide
658 using satellite (MOPITT) measurements of CO columns, *J Geophys Res Atmospheres* 1984
659 2012, 114(D4), doi:10.1029/2007JD009264, 2009.

660 Kharol, S. K., Martin, R. V., Philip, S., Boys, B., Lamsal, L. N., Jerrett, M., Brauer, M., Crouse,
661 D. L., McLinden, C. and Burnett, R. T.: Assessment of the magnitude and recent trends in
662 satellite-derived ground-level nitrogen dioxide over North America, *Atmos Environ.*, 118, 236-
663 245, doi:10.1016/j.atmosenv.2015.08.011, 2015.

664 Kopacz, M., Jacob, D., Fisher, J., Logan, J., Zhang, L., Megretskaya, I., Yantosca, R., Singh, K.,
665 Henze, D., Burrows, J., Buchwitz, M., Khlystova, I., McMillan, W., Gille, J., Edwards, D.,
666 Eldering, A., Thouret, V. and Nedelec, P.: Global estimates of CO sources with high resolution
667 by adjoint inversion of multiple satellite datasets (MOPITT, AIRS, SCIAMACHY, TES), *Atmos*
668 *Chem Phys*, 10(3), 855-876, doi:10.5194/acp-10-855-2010, 2010.

669 Kuhns, H., Green, M. and Etyemezian, V.: Big Bend Regional Aerosol and Visibility
670 Observational (BRAVO) Study Emissions Inventory, Report prepared for BRAVO Steering
671 Committee, Desert Research Institute, Las Vegas, Nevada, 2003.



672 Kumar, A., Wu, S., Weise, M. F., Honrath, R., Owen, R. C., Helmig, D., Kramer, L., Val Martin,
673 M., and Li, Q.: Free-troposphere ozone and carbon monoxide over the North Atlantic for 2001–
674 2011, *Atmos. Chem. Phys.*, 13, 12537–12547, doi:10.5194/acp-13-12537-2013, 2013.

675 Lelieveld, J., Dentener, F., Peters, W. and Krol, M.: On the role of hydroxyl radicals in the self-
676 cleansing capacity of the troposphere, *Atmos Chem Phys*, 4(9/10), 2337–2344, doi:10.5194/acp-
677 4-2337-2004, 2004.

678 Liu, F., Zhang, Q., Tong, D., Zheng, B., Li, M., Huo, H., and He, K. B.: High-resolution inventory
679 of technologies, activities, and emissions of coal-fired power plants in China from 1990 to 2010,
680 *Atmos. Chem. Phys.*, 15, 13299–13317, doi:10.5194/acp-15-13299-2015, 2015.

681 Logan, J., Megretskaya, I., Nassar, R., Murray, L., Zhang, L., Bowman, K., Worden, H. and Luo,
682 M.: Effects of the 2006 El Niño on tropospheric composition as revealed by data from the
683 Tropospheric Emission Spectrometer (TES), *Geophys Res Lett*, 35(3),
684 doi:10.1029/2007GL031698, 2008.

685 Meirink, J., Bergamaschi, P., Frankenberg, C., Amelio, M. d', Dlugokencky, E., Gatti, L.,
686 Houweling, S., Miller, J., Röckmann, T., Villani, M. and Krol, M.: Four-dimensional variational
687 data assimilation for inverse modeling of atmospheric methane emissions: Analysis of
688 SCIAMACHY observations, *J Geophys Res Atmospheres* 1984–2012, 113(D17),
689 doi:10.1029/2007JD009740, 2008.

690 Miyazaki, K., Eskes, H. and Sudo, K.: A tropospheric chemistry reanalysis for the years 2005–
691 2012 based on an assimilation of OMI, MLS, TES, and MOPITT satellite data, *Atmos Chem*
692 *Phys*, 15(14), 8315–8348, doi:10.5194/acp-15-8315-2015, 2015.

693 Montzka, S. A., Krol, M., Dlugokencky, E., Hall, B., Jöckel, P., Lelieveld, J.: Small Interannual
694 Variability of Global Atmospheric Hydroxyl, *Science*, 331(6013), 67–69,



695 10.1126/science.1197640, 2011.

696 Ohara, T., Akimoto, H., Kurokawa, J., Horii, N., Yamaji, K., Yan, X. and Hayasaka, T.: An Asian
697 emission inventory of anthropogenic emission sources for the period 1980–2020, *Atmos Chem*
698 *Phys*, 7(16), 4419–4444, doi:10.5194/acp-7-4419-2007, 2007.

699 Pfister, G., Hess, P., Emmons, L., Lamarque, J. -F., Wiedinmyer, C., Edwards, D., Pétron, G.,
700 Gille, J. and Sachse, G.: Quantifying CO emissions from the 2004 Alaskan wildfires using
701 MOPITT CO data, *Geophys Res Lett*, 32(11), doi:10.1029/2005GL022995, 2005.

702 Prinn, R., Huang, J., Weiss, R., Cunnold, D., Fraser, P., Simmonds, P., McCulloch, A., Harth, C.,
703 Reimann, S., Salameh, P., O'Doherty, S., Wang, R., Porter, L., Miller, B. and Krummel, P.:
704 Evidence for variability of atmospheric hydroxyl radicals over the past quarter century, *Geophys*
705 *Res Lett*, 32(7), n/a–n/a, doi:10.1029/2004GL022228, 2005.

706 Reddington, C., Butt, E., Ridley, D., Artaxo, P., Morgan, W., Coe, H. and Spracklen, D.: Air
707 quality and human health improvements from reductions in deforestation-related fire in Brazil,
708 *Nat Geosci*, 8(10), 768–771, doi:10.1038/ngeo2535, 2015.

709 Schnell, J. L., Prather, M. J., Josse, B., Naik, V., Horowitz, L. W., Cameron-Smith, P., Bergmann,
710 D., Zeng, G., Plummer, D. A., Sudo, K., Nagashima, T., Shindell, D. T., Faluvegi, G., and Strode,
711 S. A.: Use of North American and European air quality networks to evaluate global chemistry–
712 climate modeling of surface ozone, *Atmos. Chem. Phys.*, 15, 10581–10596, doi:10.5194/acp-15-
713 10581-2015, 2015.

714 Schneider, P., Lahoz, W. A., and van der A, R.: Recent satellite-based trends of tropospheric
715 nitrogen dioxide over large urban agglomerations worldwide, *Atmos. Chem. Phys.*, 15, 1205–
716 1220, doi:10.5194/acp-15-1205-2015, 2015.

717 Spivakovsky, C. M., Logan, J. A., Montzka, S. A., Balkanski, Y. J., Foreman-Fowler, M., Jones,



718 D. B. A., Horowitz, L. W., Fusco, A. C., Brenninkmeijer, C. A. M., Prather, M. J., Wofsy, S. C.
719 and McElroy, M. B.: Three-dimensional climatological distribution of tropospheric OH Update
720 and evaluation, *J. Geophys. Res.*, 105(D7), 8931–8980, doi:10.1029/1999JD901006, 2000.

721 Streets, D., Zhang, Q., Wang, L., He, K., Hao, J., Wu, Y., Tang, Y. and Carmichael, G.: Revisiting
722 China's CO emissions after the Transport and Chemical Evolution over the Pacific (TRACE-P)
723 mission: Synthesis of inventories, atmospheric modeling, and observations, *J. Geophys. Res.*
724 *Atmospheres* 1984–2012, 111(D14), doi:10.1029/2006JD007118, 2006.

725 Strode, S., Worden, H., Damon, M., Douglass, A., Duncan, B., Emmons, L., Lamarque, J.-F.,
726 Manyin, M., Oman, L., Rodriguez, J., Strahan, S. and Tilmes, S.: Interpreting space-based trends
727 in carbon monoxide with multiple models, *Atmos. Chem. Phys.*, 16(11), 7285–7294,
728 doi:10.5194/acp-16-7285-2016, 2016.

729 Stroppiana, D., Brivio, P. A., Grégoire, J.-M., Liousse, C., Guillaume, B., Granier, C., Mieville,
730 A., Chin, M., and Pétron, G.: Comparison of global inventories of CO emissions from biomass
731 burning derived from remotely sensed data, *Atmos. Chem. Phys.*, 10, 12173–12189,
732 doi:10.5194/acp-10-12173-2010, 2010.

733 Tan, J., Jakob, C., Rossow, W. and Tselioudis, G.: Increases in tropical rainfall driven by changes
734 in frequency of organized deep convection, *Nature*, 519(7544), 451–454,
735 doi:10.1038/nature14339, 2015.

736 Tohjima, Y., Kubo, M., Minejima, C., Mukai, H., Tanimoto, H., Ganshin, A., Maksyutov, S.,
737 Katsumata, K., Machida, T., and Kita, K.: Temporal changes in the emissions of CH₄ and CO
738 from China estimated from CH₄ / CO₂ and CO / CO₂ correlations observed at Hateruma Island,
739 *Atmos. Chem. Phys.*, 14, 1663–1677, doi:10.5194/acp-14-1663-2014, 2014.

740 Tosca, M., Diner, D., Garay, M. and Kalashnikova, O.: Human-caused fires limit convection in



741 tropical Africa: First temporal observations and attribution, *Geophys Res Lett*, 42(15), 6492–
742 6501, doi:10.1002/2015GL065063, 2015.

743 Turquety, S., Logan, J., Jacob, D., Hudman, R., Leung, F., Heald, C., Yantosca, R., Wu, S.,
744 Emmons, L., Edwards, D. and Sachse, G.: Inventory of boreal fire emissions for North America
745 in 2004: Importance of peat burning and pyroconvective injection, *J Geophys Res Atmospheres*
746 1984 2012, 112(D12), doi:10.1029/2006JD007281, 2007.

747 Turner, A. J., Jacob, D. J., Wecht, K. J., Maasakkers, J. D., Lundgren, E., Andrews, A. E., Biraud,
748 S. C., Boesch, H., Bowman, K. W., Deutscher, N. M., Dubey, M. K., Griffith, D. W. T., Hase,
749 F., Kuze, A., Notholt, J., Ohyama, H., Parker, R., Payne, V. H., Sussmann, R., Sweeney, C.,
750 Velazco, V. A., Warneke, T., Wennberg, P. O., and Wunch, D.: Estimating global and North
751 American methane emissions with high spatial resolution using GOSAT satellite data, *Atmos.*
752 *Chem. Phys.*, 15, 7049-7069, doi:10.5194/acp-15-7049-2015, 2015.

753 van der Werf, G. R., Randerson, J. T., Giglio, L., Collatz, G. J., Kasibhatla, P. S., and Arellano Jr.,
754 A. F.: Interannual variability in global biomass burning emissions from 1997 to 2004, *Atmos.*
755 *Chem. Phys.*, 6, 3423-3441, doi:10.5194/acp-6-3423-2006, 2006.

756 van der Werf, G. R., Randerson, J. T., Giglio, L., Collatz, G. J., Mu, M., Kasibhatla, P. S.,
757 Morton, D. C., DeFries, R. S., Jin, Y., and van Leeuwen, T. T.: Global fire emissions and the
758 contribution of deforestation, savanna, forest, agricultural, and peat fires (1997–2009), *Atmos.*
759 *Chem. Phys.*, 10, 11707–11735, doi:10.5194/acp-10-11707-2010, 2010.

760 van Leeuwen, T. T. and van der Werf, G. R.: Spatial and temporal variability in the ratio of trace
761 gases emitted from biomass burning, *Atmos. Chem. Phys.*, 11, 3611-3629, doi:10.5194/acp-11-
762 3611-2011, 2011.

763 Vestreng, V. and Klein, H.: Emission data reported to UNECE/EMEP. Quality assurance and trend



764 analysis and Presentation of WebDab, Norwegian Meteorological Institute, Oslo, Norway, MSC-
765 W Status Report, 2002.

766 Warner, J., Carminati, F., Wei, Z., Lahoz, W., and Attié, J.-L.: Tropospheric carbon monoxide
767 variability from AIRS under clear and cloudy conditions, *Atmos. Chem. Phys.*, 13, 12469-12479,
768 doi:10.5194/acp-13-12469-2013, 2013.

769 Worden, H., Deeter, M., Edwards, D., Gille, J., Drummond, J. and Nédélec, P.: Observations of
770 near-surface carbon monoxide from space using MOPITT multispectral retrievals, *J Geophys
771 Res Atmospheres* 1984 2012, 115(D18), doi:10.1029/2010JD014242, 2010.

772 Worden, H. M., Deeter, M. N., Frankenberg, C., George, M., Nicitiu, F., Worden, J., Aben, I.,
773 Bowman, K. W., Clerbaux, C., Coheur, P. F., de Laat, A. T. J., Detweiler, R., Drummond, J. R.,
774 Edwards, D. P., Gille, J. C., Hurtmans, D., Luo, M., Martínez-Alonso, S., Massie, S., Pfister, G.,
775 and Warner, J. X.: Decadal record of satellite carbon monoxide observations, *Atmos. Chem.
776 Phys.*, 13, 837-850, doi:10.5194/acp-13-837-2013, 2013.

777 Worden, J., Wecht, K., Frankenberg, C., Alvarado, M., Bowman, K., Kort, E., Kulawik, S., Lee,
778 M., Payne, V., and Worden, H.: CH₄ and CO distributions over tropical fires during October
779 2006 as observed by the Aura TES satellite instrument and modeled by GEOS-Chem, *Atmos.
780 Chem. Phys.*, 13, 3679-3692, doi:10.5194/acp-13-3679-2013, 2013b.

781 Worden, J., Jiang, Z., Jones, D., Alvarado, M., Bowman, K., Frankenberg, C., Kort, E., Kulawik,
782 S., Lee, M., Liu, J., Payne, V., Wecht, K. and Worden, H.: El Niño, the 2006 Indonesian peat
783 fires, and the distribution of atmospheric methane, *Geophys Res Lett*, 40(18), 4938–4943,
784 doi:10.1002/grl.50937, 2013c.

785 Xia, Y., Zhao, Y. and Nielsen, C.: Benefits of China's efforts in gaseous pollutant control indicated
786 by the bottom-up emissions and satellite observations 2000–2014, *Atmos Environ*, 136, 43–53,



787 doi:10.1016/j.atmosenv.2016.04.013, 2016.

788 Yin, Y., Chevallier, F., Ciais, P., Broquet, G., Fortems-Cheiney, A., Pison, I. and Saunois, M.:
789 Decadal trends in global CO emissions as seen by MOPITT, *Atmos Chem Phys*, 15(23), 13433–
790 13451, doi:10.5194/acp-15-13433-2015, 2015.

791 Yurganov, L. N., Duchatelet, P., Dzhola, A. V., Edwards, D. P., Hase, F., Kramer, I., Mahieu, E.,
792 Mellqvist, J., Notholt, J., Novelli, P. C., Rockmann, A., Scheel, H. E., Schneider, M., Schulz,
793 A., Strandberg, A., Sussmann, R., Tanimoto, H., Velazco, V., Drummond, J. R., and Gille, J. C.:
794 Increased Northern Hemispheric carbon monoxide burden in the troposphere in 2002 and 2003
795 detected from the ground and from space, *Atmos. Chem. Phys.*, 5, 563–573, doi:10.5194/acp-5-
796 563-2005, 2005.

797 Zhang, Q., Streets, D., Carmichael, G., He, K., Huo, H., Kannari, A., Klimont, Z., Park, I., Reddy,
798 S., Fu, J., Chen, D., Duan, L., Lei, Y., Wang, L. and Yao, Z.: Asian emissions in 2006 for the
799 NASA INTEX-B mission, *Atmos Chem Phys*, 9(14), 5131–5153, doi:10.5194/acp-9-5131-2009,
800 2009.

801 Zhang, L., Li, Q. B., Jin, J., Liu, H., Livesey, N., Jiang, J. H., Mao, Y., Chen, D., Luo, M., and
802 Chen, Y.: Impacts of 2006 Indonesian fires and dynamics on tropical upper tropospheric carbon
803 monoxide and ozone, *Atmos. Chem. Phys.*, 11, 10929–10946, doi:10.5194/acp-11-10929-2011,
804 2011.

805 Zhao, Y., Nielsen, C., McElroy, M., Zhang, L. and Zhang, J.: CO emissions in China: Uncertainties
806 and implications of improved energy efficiency and emission control, *Atmos Environ*, 49, 103–
807 113, doi:10.1016/j.atmosenv.2011.12.015, 2012.

808

809 **Tables and Figures**



810 **Table 1.** Annual total anthropogenic CO emission in different regions, from 2001 to 2015,
811 constrained with MOPITT column, profile and lower tropospheric data. The region definition is
812 shown in Figure 2e.
813

814 **Figure 1.** Difference between MOPITT CO retrievals and HIPPO aircraft measurements. The
815 aircraft measurements are smoothed with MOPITT averaging kernels. The black solid line shows
816 the 4-order polynomial curve fitting, which is used to correct MOPITT data in this work.
817

818 **Figure 2.** (a-d) Mean a priori CO emissions from combustion sources and the oxidation of biogenic
819 VOCs and CH₄ from 2001 to 2015. The unit is 10¹² molec/cm²/sec. (e-f) Region definitions for (e)
820 anthropogenic and (f) biomass burning sources.
821

822 **Figure 3.** Schematic diagram for methodology of the assimilation system. Sequential Kalman
823 Filter was run from March 1 2000 to December 31 2015 to produce the optimized initial conditions
824 (monthly) and boundary conditions (hourly). Monthly 4-DVAR inversions were performed with
825 the optimized initial conditions. Only MOPITT data over land (white grids) were assimilated in
826 the 4-DVAR inversions, while the CO abundances over ocean (red grids) were defined as
827 boundaries and rewritten using the optimized hourly CO fields from Kalman Filter.
828

829 **Figure 4.** (a) Locations of WDCGG sites with MCF measurements. (b) Global mean MCF
830 concentration. (c) Exponential loss rate of MCF, derived from 12-month apart of monthly means
831 [e.g., ln(MCF_{Jan2007}/MCF_{Jan2006})]. The black solid line shows the 12-month mean value.
832

833 **Figure 5.** CO emission trends for 2001 – 2015, constrained with MOPITT column, profile and
834 lower tropospheric profile data. The months dominated by biomass burning emissions are excluded
835 from the trend calculation for anthropogenic and biogenic VOC emissions.
836

837 **Figure 6.** 12-month mean value of anthropogenic CO emissions (with unit Tg/month) for 2001 –
838 2015: a priori emission (green) and a posteriori emissions constrained with MOPITT column data
839 (black), MOPITT profile data (blue) and MOPITT lower tropospheric profile data (red). The green
840 dash line shows the monthly a priori anthropogenic CO emissions. The region definition is shown
841 in Figure 2e.
842

843 **Figure 7.** Monthly mean CO concentrations (green) and 12-month mean value (black) from
844 WDCGG stations for 2001 – 2015. (a) 15-station average in United States (b) 20-station average
845 in Europe (c) 2-station (YON and JMA) average in east China outflow (4) Cape Rama (CRI) in
846 India.
847

848 **Figure 8.** Monthly biomass burning CO emissions (with unit Tg/month) for 2001 – 2015: a priori
849 emission (green) and a posteriori emissions constrained with MOPITT column data (black),
850 MOPITT profile data (blue) and MOPITT lower tropospheric profile data (red). The region
851 definition is shown in Figure 2f.
852

853 **Figure 9.** Panels (a-d): long-term trend (annual) of surface CO concentration for 2001 – 2015 from
854 WDCGG sites, and model simulations driven with a priori and a posteriori emissions. Panels (e-
855 g): effect of a posteriori emissions, derived by abs(Trend_{aposteriori} – Trend_{WDCGG}) - abs(Trend_{apriori} -



856 Trend_{WDCGG}); blue (red) means the a posteriori emissions improves (degrades) the agreement with
857 WDCGG measurements compared to the a priori emissions, while white indicates no change from
858 the priori. Only stations with more than 10 year observations (the time range between the first and
859 last observations) during 2001-2015 are included.
860

861 **Figure 10.** Panels (a-d): long-term mean value of surface CO concentration for 2001 – 2015 from
862 WDCGG sites, and model simulations driven with a priori and a posteriori emissions. Panels (e-
863 g): effect of a posteriori emissions, derived by $\text{abs}(\text{CO}_{\text{aposteriori}} - \text{CO}_{\text{WDCGG}}) - \text{abs}(\text{CO}_{\text{apriori}} -$
864 $\text{CO}_{\text{WDCGG}})$; blue (red) means the a posteriori emissions improves (degrades) the agreement with
865 WDCGG measurements compared to the a priori emissions, while white indicates no change from
866 the priori. Only stations with more than 10 year observations (the time range between the first and
867 last observations) during 2001-2015 are included.
868

869 **Figure 11.** Long-term trend (annual) of modeled surface and column CO for 2001 – 2015 with (a-
870 b) all emission sources are fixed at 2001 level. (c-d) variable anthropogenic emissions; (e-f)
871 variable biomass burning emissions; (g-h) variable biogenic VOCs emissions; The variable
872 emissions are constrained with MOPITT profile data.



Years	MOPITT Column (Tg/year)				MOPITT Profile (Tg/year)				MOPITT Lower Profile (Tg/year)			
	United States	Europe	E China	India/SE Asia	United States	Europe	E China	India/SE Asia	United States	Europe	E China	India/SE Asia
2001	87.8	71.6	165.7	102.2	87.7	77.3	170.4	97.5	112.9	92.0	215.7	136.1
2002	84.1	65.9	171.3	93.3	82.3	77.1	176.1	81.1	110.1	89.8	221.9	119.8
2003	80.8	65.3	178.8	95.4	80.4	74.5	189.2	88.5	103.6	87.0	218.1	121.9
2004	77.4	65.5	178.5	105.0	91.1	83.8	205.6	113.8	103.0	89.5	222.8	124.6
2005	72.7	64.6	178.6	104.3	82.6	79.4	200.6	116.8	92.7	84.5	215.3	126.2
2006	74.6	61.5	172.7	98.1	85.6	74.5	197.7	111.0	93.9	78.9	205.1	118.1
2007	73.7	56.5	177.1	105.8	84.0	67.9	200.9	113.2	90.9	71.8	208.1	119.4
2008	67.1	55.5	150.2	102.1	77.2	65.4	175.4	110.2	83.9	69.6	175.0	111.1
2009	66.0	54.8	162.0	105.7	74.5	65.1	185.9	118.3	78.0	67.0	184.5	115.1
2010	59.2	54.5	159.3	100.5	67.8	65.3	183.1	112.8	73.5	69.0	185.5	106.7
2011	53.5	52.9	153.2	107.4	60.5	63.1	179.5	120.3	63.0	65.6	175.7	107.5
2012	54.9	58.3	167.0	113.8	58.2	65.2	184.2	128.8	62.5	68.9	187.0	115.7
2013	54.3	62.6	160.4	120.9	56.7	68.8	171.2	131.3	61.8	73.8	176.8	114.6
2014	55.0	60.1	157.1	121.3	56.8	63.9	175.6	133.4	60.9	68.5	174.4	115.5
2015	55.1	61.4	145.1	115.6	56.8	66.9	159.0	130.4	59.5	69.3	160.5	109.2

873

874 **Table 1.** Annual total anthropogenic CO emission in different regions, from 2001 to 2015,
875 constrained with MOPITT column, profile and lower tropospheric data. The region definition
876 is shown in Figure 2e.

877

878

879

880

881

882

883

884

885

886

887

888

889

890

891

892

893

894

895

896

897

898

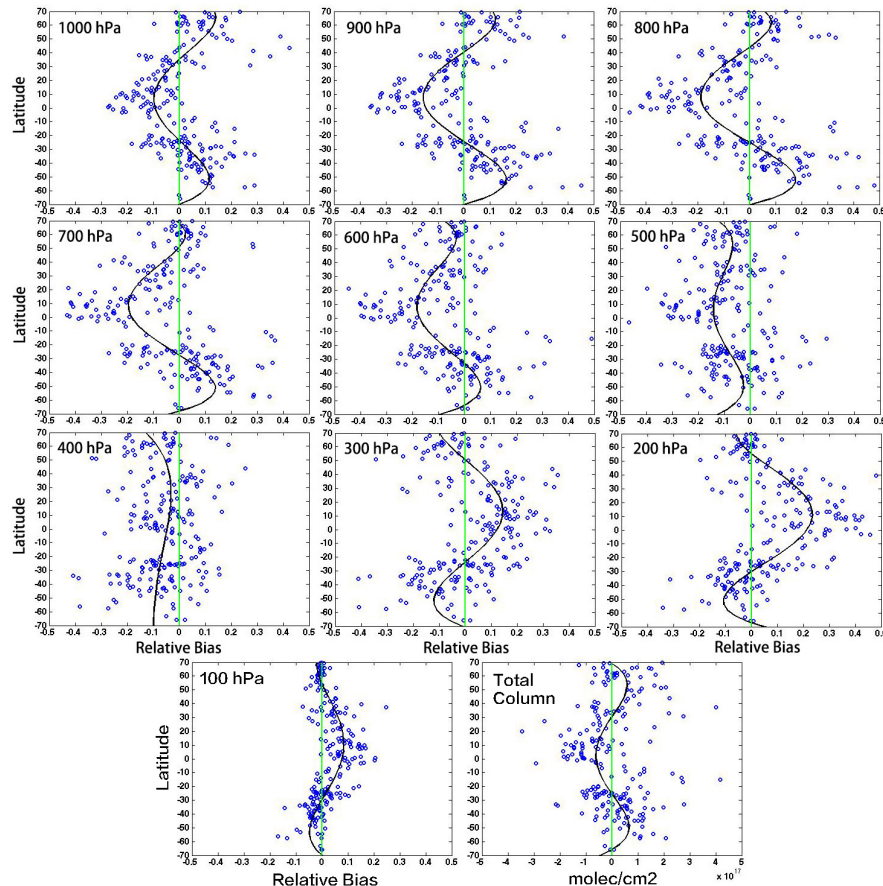
899

900

901

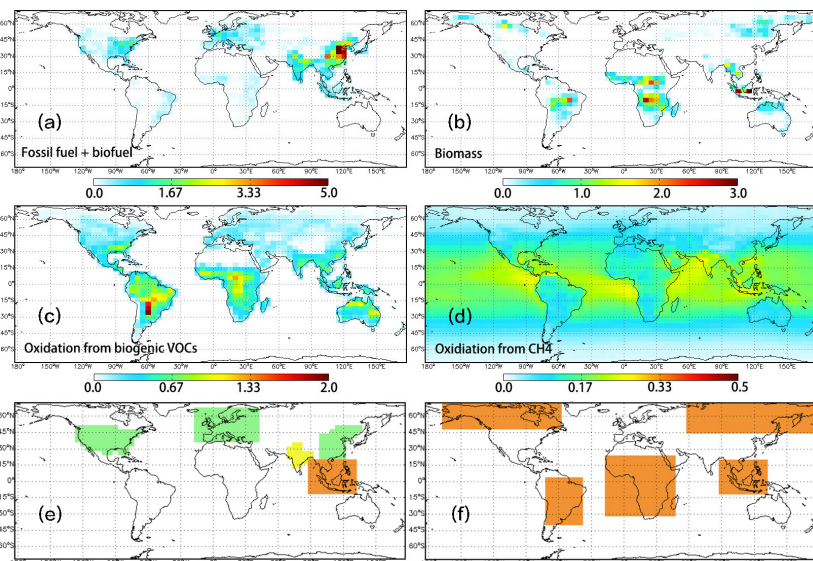


902
903
904
905
906
907



908
909
910
911
912
913
914
915
916
917
918

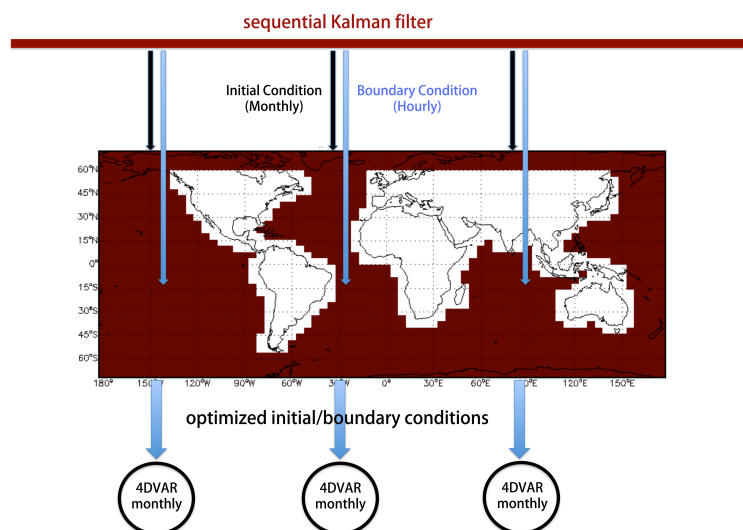
Figure 1. Difference between MOPITT CO retrievals and HIPPO aircraft measurements. The aircraft measurements are smoothed with MOPITT averaging kernels. The black solid line shows the 4-order polynomial curve fitting, which is used to correct MOPITT data in this work.



919

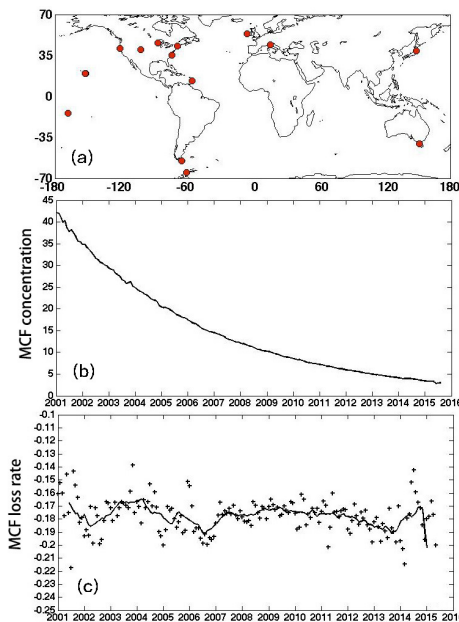
920 **Figure 2.** (a-d) Mean a priori CO emissions from combustion sources and the oxidation of
 921 biogenic VOCs and CH₄ from 2001 to 2015. The unit is 10¹² molec/cm²/sec. (e-f) Region
 922 definitions for (e) anthropogenic and (f) biomass burning sources.

923



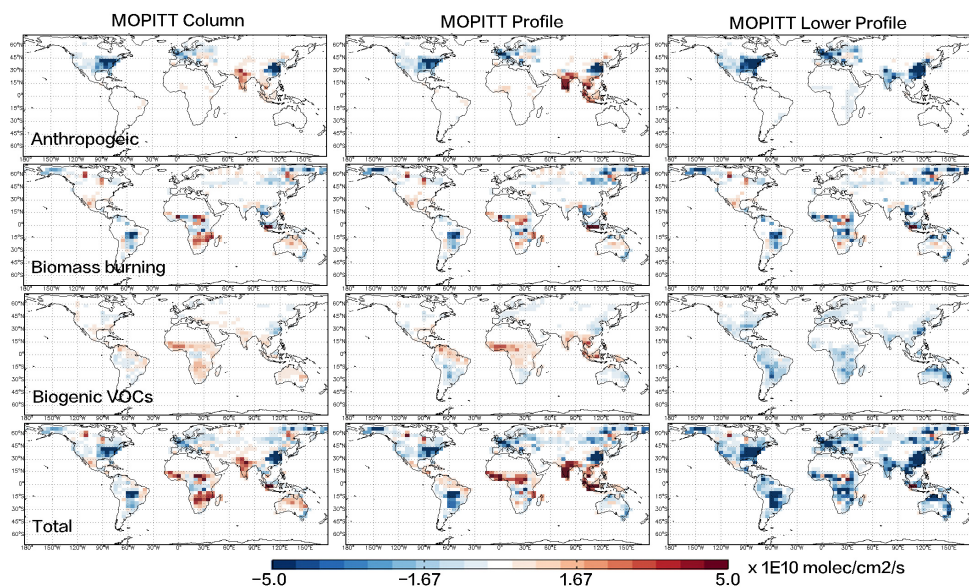
924

925 **Figure 3.** Schematic diagram for methodology of the assimilation system. Sequential Kalman
 926 Filter was run from March 1 2000 to December 31 2015 to produce the optimized initial
 927 conditions (monthly) and boundary conditions (hourly). Monthly 4-DVAR inversions were
 928 performed with the optimized initial conditions. Only MOPITT data over land (white grids)
 929 were assimilated in the 4-DVAR inversions, while the CO abundances over ocean (red grids)
 930 were defined as boundaries and rewritten using the optimized hourly CO fields from Kalman
 Filter.



931

932 **Figure 4.** (a) Locations of WDCGG sites with MCF measurements. (b) Global mean MCF
933 concentration. (c) Exponential loss rate of MCF, derived from 12-month apart of monthly
934 means [e.g., $\ln(MCF_{Jan2007}/MCF_{Jan2006})$]. The black solid line shows the 12-month mean value.
935

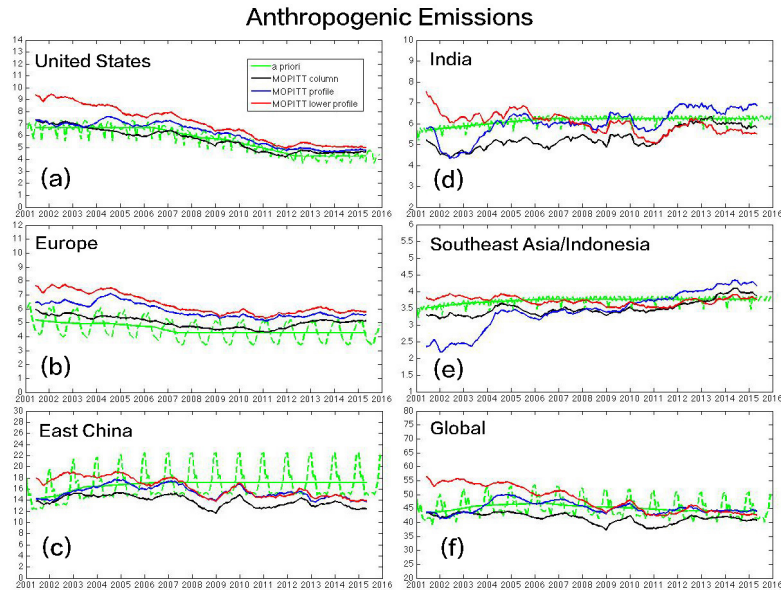


936

937 **Figure 5.** CO emission trends for 2001 – 2015, constrained with MOPITT column, profile and
938 lower tropospheric profile data. The months dominated by biomass burning emissions are
939 excluded from the trend calculation for anthropogenic and biogenic VOC emissions.



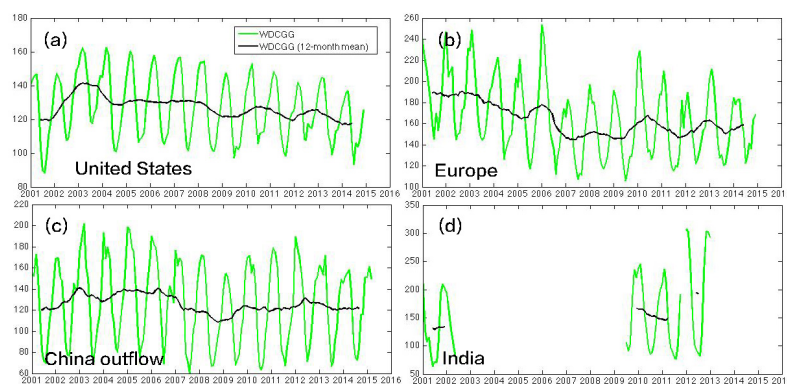
940



941

942 **Figure 6.** 12-month mean value of anthropogenic CO emissions (with unit Tg/month) for 2001
 943 – 2015: a priori emission (green) and a posteriori emissions constrained with MOPITT column
 944 data (black), MOPITT profile data (blue) and MOPITT lower tropospheric profile data (red).
 945 The green dash line shows the monthly a priori anthropogenic CO emissions. The region
 946 definition is shown in Figure 2e.
 947

948



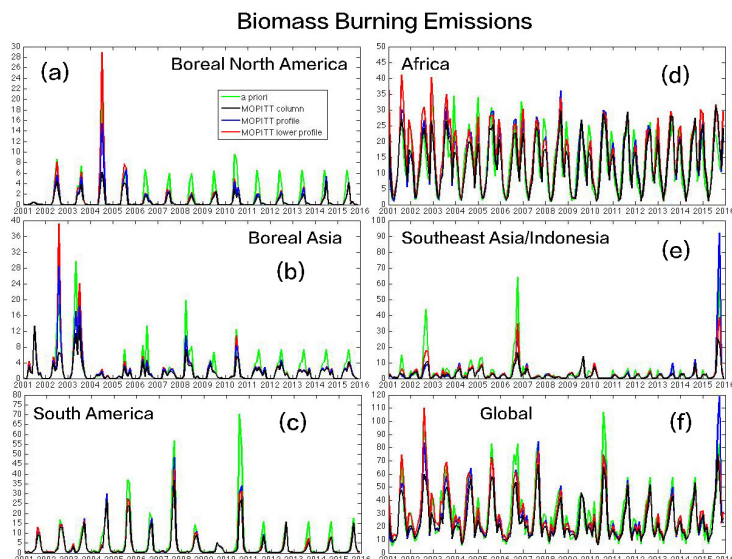
949

950 **Figure 7.** Monthly mean CO concentrations (green) and 12-month mean value (black) from
 951 WDCGG stations for 2001 – 2015. (a) 15-station average in United States (b) 20-station
 952 average in Europe (c) 2-station (YON and JMA) average in east China outflow (4) Cape Rama
 953 (CRI) in India.
 954

955



956
957
958
959
960
961
962
963
964
965
966
967

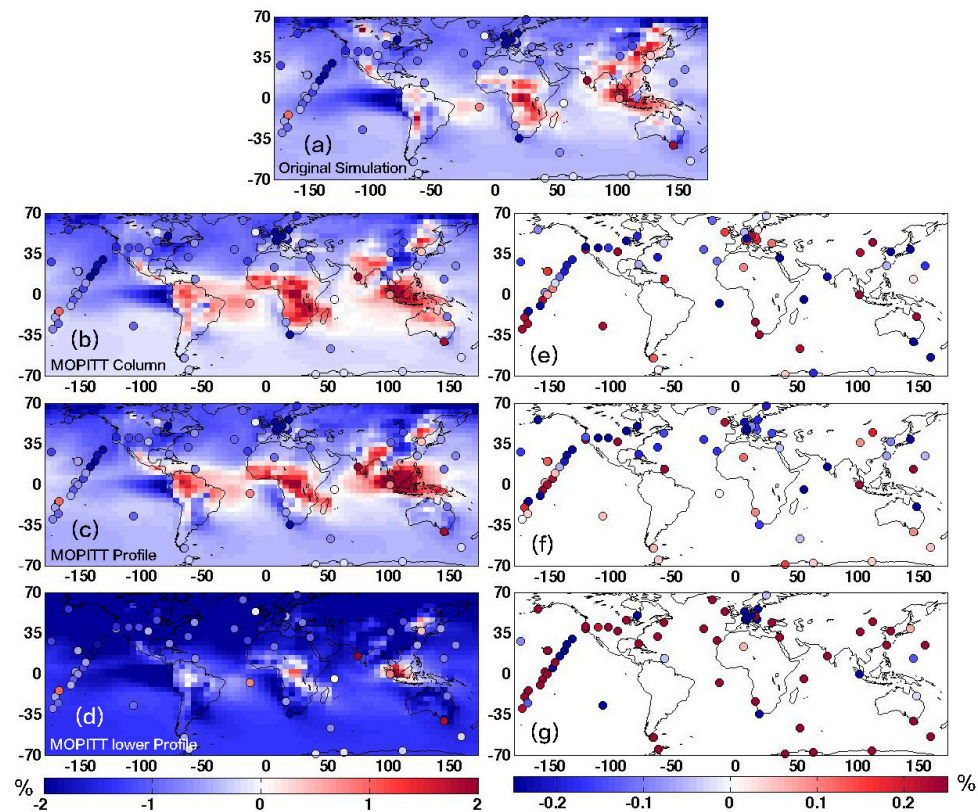


968
969
970
971
972
973
974
975
976
977
978
979
980
981
982
983

Figure 8. Monthly biomass burning CO emissions (with unit Tg/month) for 2001 – 2015: a priori emission (green) and a posteriori emissions constrained with MOPITT column data (black), MOPITT profile data (blue) and MOPITT lower tropospheric profile data (red). The region definition is shown in Figure 2f.



984
985
986
987
988



989

990 **Figure 9.** Panels (a-d): long-term trend (annual) of surface CO concentration for 2001 – 2015
991 from WDCGG sites, and model simulations driven with a priori and a posteriori emissions.
992 Panels (e-g): effect of a posteriori emissions, derived by $\text{abs}(\text{Trend}_{\text{a posteriori}} - \text{Trend}_{\text{WDCGG}}) -$
993 $\text{abs}(\text{Trend}_{\text{a priori}} - \text{Trend}_{\text{WDCGG}})$; blue (red) means the a posteriori emissions improves (degrades)
994 the agreement with WDCGG measurements compared to the a priori emissions, while white
995 indicates no change from the priori. Only stations with more than 10 year observations (the
996 time range between the first and last observations) during 2001-2015 are included.

997

998

999

1000

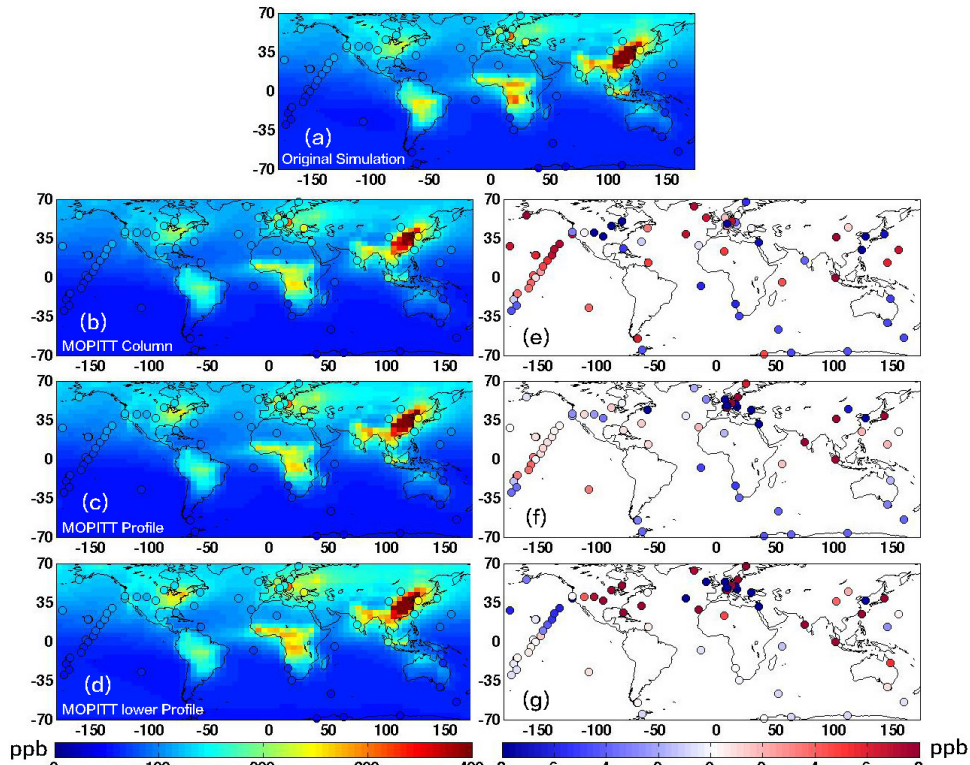
1001

1002

1003



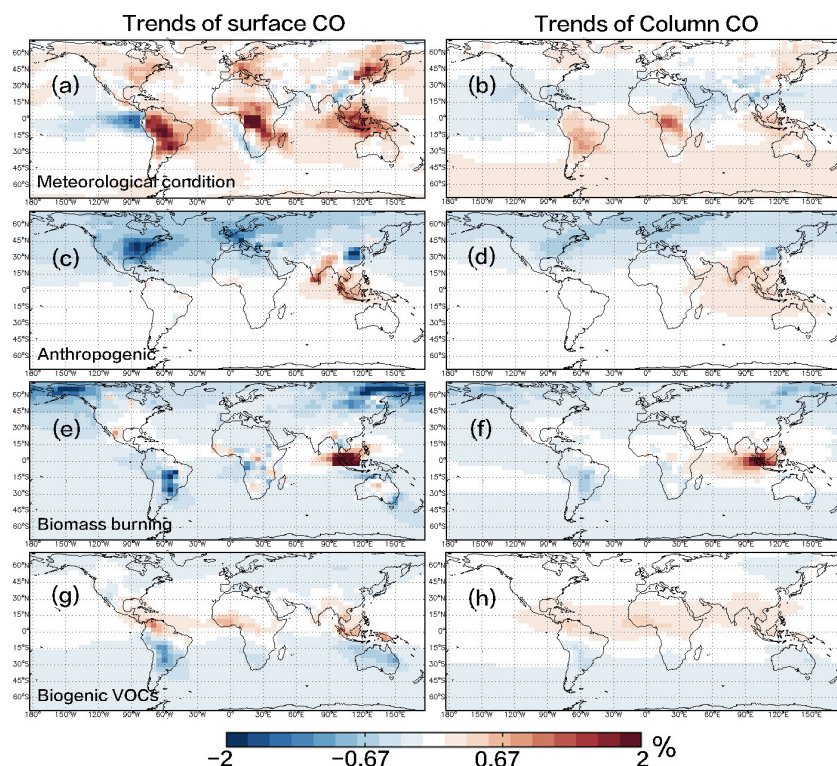
1004
1005
1006
1007
1008



1009
1010 **Figure 10.** Panels (a-d): long-term mean value of surface CO concentration for 2001 – 2015
1011 from WDCGG sites, and model simulations driven with a priori and a posteriori emissions.
1012 Panels (e-g): effect of a posteriori emissions, derived by $\text{abs}(\text{CO}_{\text{aposteriori}} - \text{CO}_{\text{WDCGG}}) -$
1013 $\text{abs}(\text{CO}_{\text{apriori}} - \text{CO}_{\text{WDCGG}})$; blue (red) means the a posteriori emissions improves (degrades) the
1014 agreement with WDCGG measurements compared to the a priori emissions, while white
1015 indicates no change from the priori. Only stations with more than 10 year observations (the
1016 time range between the first and last observations) during 2001-2015 are included.
1017
1018
1019
1020
1021
1022
1023
1024



1025
1026
1027
1028
1029
1030
1031
1032



1033
1034
1035
1036
1037

Figure 11. Long-term trend (annual) of modeled surface and column CO for 2001 – 2015 with (a-b) all emission sources are fixed at 2001 level. (c-d) variable anthropogenic emissions; (e-f) variable biomass burning emissions; (g-h) variable biogenic VOCs emissions; The variable emissions are constrained with MOPITT profile data.